Cobalt epitaxial nanoparticles on CaF_2/Si(111): Growth process, morphology, crystal structure, and magnetic properties

N. S. Sokolov,[1,*] S. M. Suturin,[1] B. B. Krichevtsov,[1] V. G. Dubrovskii,[1,2] S. V. Gastev,[1] N. V. Sibirev,[2] D. A. Baranov,[1] V. V. Fedorov,[1] A. A. Sitnikova,[1] A. V. Nashchekin,[1] V. I. Sakharov,[1] I. T. Serenkov,[1] T. Shimada,[3] T. Yanase,[3] and M. Tabuchi[4]

[1]*Ioffe Physical Technical Institute of the Russian Academy of Sciences, Polytekhnicheskaya 26, 194021 St. Petersburg, Russia*

[2]*St. Petersburg Academic University, Khlopina 8/3, 194021 St. Petersburg, Russia*

[3]*Division of Materials Chemistry, Faculty of Engineering, Hokkaido University, Sapporo, Hokkaido 060-8628, Japan*

[4]*Synchrotron Radiation Research Center, Nagoya University, Furo-cho, Chikusa-ku, Nagoya 464-8603, Japan*

(Received 17 November 2012; revised manuscript received 1 February 2013; published 7 March 2013)

We study molecular beam epitaxy growth, morphology, crystal structure, and magnetic properties of Co nanoislands on CaF_2/Si(111) surface. In order to have a full appreciation of complex growth kinetics at different stages, a comprehensive study of Co growth on CaF_2 is carried out by atomic force, scanning electron, and transmission electron microscopies in the direct space, as well as by x-ray and electron diffraction in the reciprocal space. These experimental data are complemented by theoretical modeling. Magnetic properties are characterized by magneto-optical Kerr effect and superconducting quantum interference device magnetometries. Key effects influencing the Co growth on fluorite are addressed, including the sticking probability, the preferential nucleation sites, the size and shape time evolution, the dependence of Co morphology on temperature and Co exposure, and the coalescence mechanism. The two-stage deposition technique is developed, whereby the low-temperature seeding stage is used to facilitate Co nucleation, and the follow-up high-temperature deposition yields Co particles with high crystalline quality. Our results enable precise control over the resulting morphology, spatial ordering, and crystal structure affecting the magnetic properties. In particular, it is demonstrated that the transformation from dense to isolated Co nanoparticles leads to the change of the in-plane and out-of-plane magnetic anisotropy and also the sign of polar and longitudinal magneto-optical Kerr effects.

DOI: 10.1103/PhysRevB.87.125407 PACS number(s): 81.15.Hi, 75.75.Fk, 81.10.Aj

I. INTRODUCTION

Nucleation and growth of different metals on insulating surfaces have been of interest for a long time. Much higher surface energy of metals than that of insulators results in the Volmer-Weber growth mode whereby three-dimensional (3D) metal islands nucleate on the surface directly, without forming any wetting layer in between. The best known systems of this type are noble metals on alkali halides.[1,2] It has been found that, although single-metal adatoms easily desorb from the halide surface above room temperature, they can also form irreversibly growing nuclei by joining other adatoms or small clusters via the surface diffusion process. Considerable attention has been paid to growing metals on oxides such as TiO_2,[3,4] MgO,[5] NiO,[6] and $SrTiO_3$.[7] Depending on the substrate preparation procedure and the growth conditions used, predominant nucleation at the surface steps or on planar terraces was observed. For the best studied TiO_2(110) surface, it has been shown that the critical cluster size is much larger compared to metal surfaces and exceeds ten atoms in the Ni/TiO_2(100) system.[4] Another interesting feature observed in the Ni/TiO_2(100) and Cu/TiO_2(100) systems is the so-called self-limiting growth mode, in which the island density linearly increases with the coverage at the initial stage and then reaches a certain saturation density where metal clusters start growing vertically.[4,8]

Much less is known about the growth properties of metals on alkaline-earth fluorides. Growth of Fe, Co, and Ag on the CaF_2(111) surface via a rather specific defect-induced nucleation mode was reported in Ref. 9. However, no epitaxial relationship to the substrate was shown under these particular growth conditions. Epitaxial growth of the α-Fe(110) on the CaF_2(111) surface was reported in Ref. 10, where the epitaxial relations Fe(110)$\|CaF_2$(111) and Fe[1-10]$\|CaF_2$[1-21] were established by x-ray diffraction. Later on, epitaxial growth of Co nanoparticles on the CaF_2(111) and CaF_2(110) surfaces was confirmed by *in situ* reflection high-energy electron diffraction (RHEED).[11,12] Since Co segregates into an ensemble of 3D islands with a modest coverage on insulating surfaces and forms a two-dimensional continuous layer on metal surfaces, there is a drastic difference between magnetic properties of the same amount of Co deposited onto an insulator or metal.[13–15] Ferromagnetic metals on insulators showing pronounced antiferromagnetic ordering are of particular interest in connection with physics and applications of the exchange bias effect.[16,17] Since magnetic properties of Co on insulating substrates are expected to be strongly dependent on the surface morphology of 3D islands, it is paramount to identify kinetic tuning knobs enabling a precise control over the size distribution of the self-induced Co nanoparticles during growth.

In this work, we present a systematic study of growth, structural, and magnetic properties of Co nanoparticles on atomically clean CaF_2(111) surfaces in a wide range of growth parameters. Growth is performed by molecular beam epitaxy (MBE) technique. Our structural characterization methods include RHEED, atomic force microscopy (AFM), scanning electron microscopy (SEM), transmission electron microscopy (TEM), medium energy ions scattering (MEIS), and grazing incidence x-ray diffraction (XRD). Magnetic properties are studied by applying the magneto-optical Kerr effect as well as superconducting quantum interference device (SQUID)

measurements. We show that the deposition of Co onto a clean and atomically flat $CaF_2(111)$ surface results in the formation of ensembles of epitaxial 3D nanoparticles. Their density and size can be tuned in a wide range by changing the substrate temperature and the Co exposure. We develop theoretical models that explain quite well the observed growth behavior. The models are based on the kinetic approach used previously in modeling the formation of the Stranski-Krastanow islands in lattice mismatched material systems.[18]

By using Si substrates with a small miscut angle and growing a low-temperature seeding layer at the initial stage, Co nanoparticles can be organized into linear chains. This gives rise to a distinct anisotropy of magnetic properties. The observed geometrical shapes of Co nanoparticles are in agreement with the dominant face-centered-cubic (fcc) crystal structure. It will be shown that the transition from a dilute ensemble of magnetically isolated nanoparticles to an almost continuous film leads to a drastic change of magnetic and magneto-optical properties.

The paper is organized as follows. Experimental techniques are described in Sec. II. Experimental results on the nucleation and growth processes of Co nanoparticles, along with the related modeling, are presented in Sec. III. Section IV treats the crystal structure, epitaxial relations, and structural defects of Co nanoparticles. Shapes of Co nanoparticles are analyzed in Sec. V. Section VI is dedicated to studies of magnetic properties of Co arrays. The main results of this work are summarized in Sec. VII.

II. EXPERIMENTAL TECHNIQUES

MBE growth of $Co/CaF_2/Si(111)$ samples was carried out in a dedicated ultrahigh-vacuum (UHV) system. Slightly off-cut silicon substrates (with misorientation angles of less than 15 angular minutes) were first cleaned by the conventional Shiraki chemical treatment and then flash annealed in an UHV chamber at 1200 °C to remove the oxide. Distinct 7×7 patterns originating from a clean Si(111) surface were observed by RHEED. Growth of a CaF_2 buffer layer on Si was performed from an effusion cell with a graphite crucible loaded with pieces of CaF_2 crystals. The CaF_2 deposition rate was calibrated to 2–3 nm/min by using an Inficon quartz thickness monitor. Cobalt was then deposited on top of a CaF_2 buffer layer from an *e*-beam source (SVT Associates, Inc.) where the target was a Co rod with a 6-mm diameter. The cobalt flux was usually kept at 0.2–0.3 nm/min. The substrate temperature during the cobalt deposition was varied from room temperature to 700 °C, while the Co exposure was changed between 0.1 and 45 nm. Here and below, we define the Co exposure D as the thickness of an imaginary flat Co layer that would form in the absence of desorption and nucleation. This value is equivalent to the flux measured by the quartz thickness monitor (mass per unit time per unit area divided by the Co density), multiplied by the growth time. In some experiments, a low-temperature Co seeding layer with the exposure of less than one monolayer was grown at a low T (between room temperature and 200 °C) before depositing Co at elevated temperatures, in order to increase the number of nucleation sites.

The AFM images were obtained with an ambient-air NT-MDT microscope operating in the semicontact mode. SEM studies were performed in a JSM 7001F (JEOL) microscope operating in the secondary electron regime. High-resolution TEM (HRTEM) studies were carried out using a JEOL 2100F microscope at an accelerating potential of 200 kV. The samples for HRTEM studies were prepared by standard methods involving ion sputtering at the last stage. MEIS studies were carried out using a setup described in detail in Ref. 19. Some samples were additionally studied by XRD at BL3A beamline of the Photon Factory synchrotron (Tsukuba, Japan). The measurements were performed on a Huber four-circle diffractometer with either a YAP scintillating point detector or a Hamamatsu two-dimensional charge-coupled device (CCD) detector. To increase the surface sensitivity, grazing incidence geometry was used with an incident angle of 2°–5°. Magnetic properties of the ensembles of Co nanoparticles were characterized by measurements of longitudinal (LMOKE) as well as polar (PMOKE) magneto-optical Kerr effect at room temperature using a laser operating at 633 nm. High sensitivity of LMOKE measurements ($\Delta\alpha \sim 1$ μrad) was achieved through a sweeping magnetic field at 1 Hz and averaging over 10–100 cycles depending on the observed signal-to-noise ratio. Magnetic moments of the samples were measured using a Quantum Design MPMS XL SQUID magnetometer.

III. NUCLEATION AND GROWTH OF Co NANOPARTICLES ON $CaF_2(111)$ SURFACE

Aiming at studies of Co nucleation and growth on a morphologically ordered and defect-free $CaF_2(111)$ surface, special care has been taken to optimize the growth of a fluorite buffer layer on silicon substrates. We have found that the most regular surface morphology of CaF_2 is obtained with the two-stage growth procedure. During the first, low-temperature stage (1 nm of CaF_2 deposited at a surface temperature of 250 °C), a thin fluorite layer uniformly covers the Si surface without changing its step structure. The second, high-temperature stage (6–7 nm deposited at 770 °C) yields relatively wide terraces with the average spacing close to that of the initial off-cut Si(111) substrate. Using this procedure,

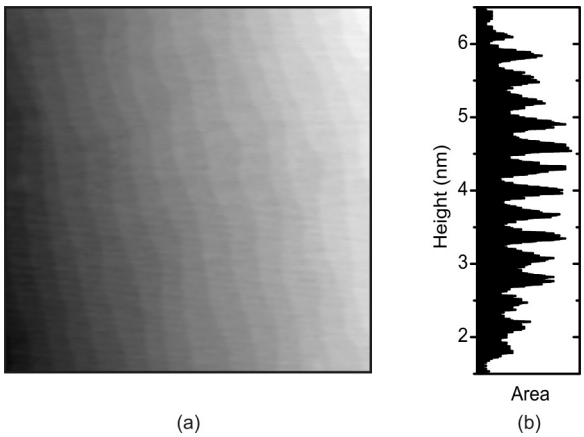

FIG. 1. Calcium fluoride buffer layer grown on a slightly off-cut Si(111) substrate by the two-step technique: (a) AFM image; size 1400 nm × 1400 nm × 6 nm. (b) The calculated height histogram showing the terrace-related peaks that correspond to ~0.31-nm step height.

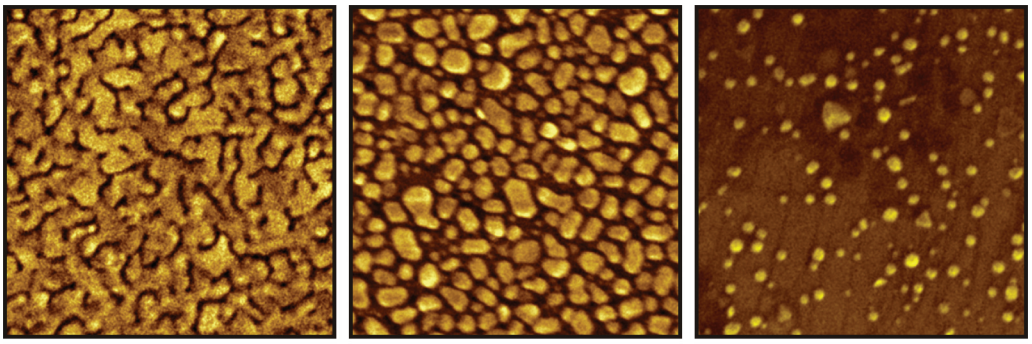

FIG. 2. (Color online) SEM images of samples grown at 100 °C (a), 300 °C (b), and 500 °C (c) at a Co exposure of 20 nm. The image size is 800 nm × 800 nm.

we avoid the formation of triangular pits that are typical for the high-temperature CaF_2 growth on Si(111) and suppress surface roughening caused by shortening the CaF_2 terraces at moderate growth temperatures (650 °C–700 °C).[20] The RHEED patterns during and after growth show narrow streaks revealing high crystal quality and flatness of the surface. It is worth mentioning that, during the low-temperature stage, the crystallographic axes of CaF_2 and Si are co-oriented, corresponding to the so-called A-type epitaxial relations at the CaF_2/Si(111) interface, which transforms into the B-type (rotated by 180°) interface right after the temperature increase above 500 °C.[21] A typical AFM image shown in Fig. 1(a) confirms that the two-stage growth technique results in a uniform CaF_2 layer with smooth monoatomic steps. The step height of ∼0.31 nm can be estimated from the height distribution histogram shown in Fig. 1(b).

A. Role of growth temperature and Co exposure

In order to study systematically the dependence of the island morphology on the growth temperature and Co exposure, a variety of samples were grown at different T from room temperature up to 700 °C and exposures varying from 1 to 40 nm, and analyzed by AFM and SEM. In particular, Fig. 2 shows the SEM images of three samples grown with a fixed exposure of 20 nm at 100 °C, 300 °C, and 500 °C, respectively. It is clearly seen that the total surface area occupied by Co decreases drastically with temperature. To measure the total volume of Co on the surface, MEIS measurements were carried out. It has been found that 100% of cobalt remains on the surface at 100 °C (the complete condensation regime), decreasing to a 51% fraction at 300 °C and to only 8% at 500 °C (the incomplete condensation regime). These values give the sticking coefficient integrated over the entire growth time. More precisely, two different processes should be distinguished. The first one involves sticking of Co on CaF_2, a heterogeneous metal-insulator process in which the sticking coefficient is expected to be strongly temperature dependent. The second process is the direct impingement of Co on Co with almost 100% sticking probability in our temperature window. At the nucleation stage where the Co coverage is very low, the Co-CaF_2 sticking is always dominant. As the coverage increases, more and more of the arriving Co atoms directly impinge the island's surface and stick to it with 100% probability.

Experimental height-exposure $[H(D)]$ dependences measured by AFM for different Co growth temperatures are shown in Fig. 3 and feature a qualitatively different behavior. At 100 °C, the island height increases sublinearly with the exposure and can be well fitted by the power-law dependence $H = aD^{1/3}$ with $a = 5$ nm$^{2/3}$, while the dependence at 500 °C is linear: $H = bD$ with $b = 1.05$. The observed

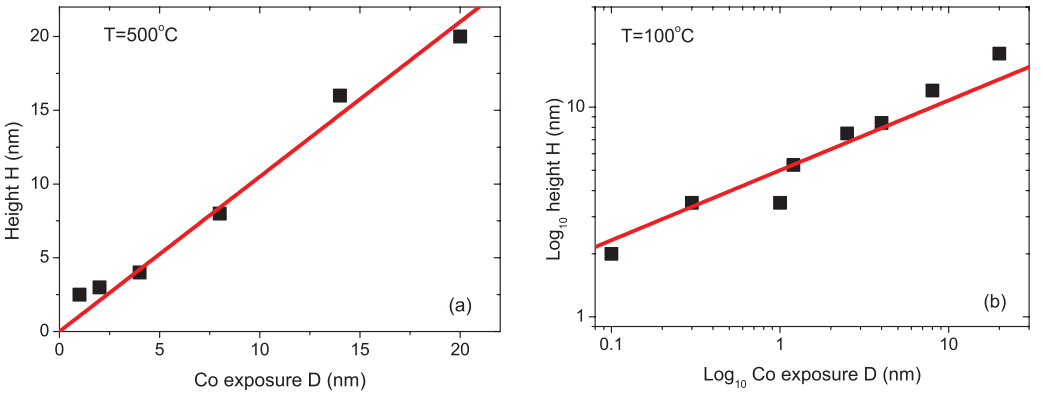

FIG. 3. (Color online) Measured dependences of the island height on the Co exposure at 500 °C (a) and 100 °C (b) (symbols), fitted by the power-law dependences discussed in the main text (lines).

difference can be explained by different kinetic mechanisms of island growth.[1,22–24] Indeed, the surface diffusion length of Co should be smaller at higher temperatures due to reevaporation. Therefore, the islands grow primarily by the direct impingement of Co atoms onto their surface. For a 3D island with a time-independent shape, the growth rate of its volume (expressed in the number of atoms per unit time), di/dt, is given by

$$\frac{di}{dt} = JC_1H^2, \tag{1}$$

where J is the arrival rate (per unit area per second) from vapor and C_1 is the shape constant such that C_1H^2 is the island cross section intercepted by the molecular beam. Since $i = (C_2H^3)/\Omega$, where C_2 is the shape constant such that C_2H^3 is the island volume and Ω is the elementary volume in the solid phase, and the Co exposure $D = J\Omega t$ by definition, integration of Eq. (1) leads to a linear dependence of the island height on the Co exposure,

$$H = \frac{C_1}{3C_2}D. \tag{2}$$

This corresponds to the high-temperature growth law at 500 °C shown in Fig. 3(a). Islands at 100 °C should be mainly fed from the surface, because the Co diffusion length at this low temperature is much larger.[23,24] Possible mechanisms of mass transport into the islands include the normal diffusion of adsorbed Co by random migration on a planar terrace and the diffusion along the surface step. Since islands grow by consuming the surface adatoms, the surface supersaturation rapidly tends to zero.[22–24] Whatever is the growth mechanism, the mass conservation yields the material balance of the form[24]

$$D \cong D_{eq} + \Omega Ni. \tag{3}$$

Here, D_{eq} denotes the residual equilibrium Co coverage of the surface, and the last term on the right-hand side gives the total volume of islands per unit area in the monodispersive approximation of the island size distribution with N as the island surface density. Assuming that $D \gg D_{eq}$ (this inequality should always pertain for the Volmer-Weber growth) and using the relationship between i and H, we obtain

$$H \cong \left(\frac{D}{C_2N}\right)^{1/3}, \tag{4}$$

which explains the dependence shown in Fig. 3(b).

Figure 4 shows the dependences of the island density on the Co exposure at different temperatures. It is seen that the density is dramatically affected by the growth temperature. At a fixed exposure of 10 nm, the density of islands grown at 500 °C is two orders of magnitude lower than at 200 °C. Lines in Fig. 4 represent theoretical fits obtained from the model of stress-driven 3D islanding of Refs. 23 and 24. In brief, the model describes the nucleation of 3D islands under a deposition flux with neglect of island interaction, e.g., elastic interaction or coalescence. By applying the approach based on classical nucleation theory in the deterministic limit (i.e., disregarding the fluctuation-induced effects at a short-scale nucleation stage),[22] the resulting size distribution has a time-invariant double exponential shape in terms of the invariant size (for which the island growth rate is size independent).[22]

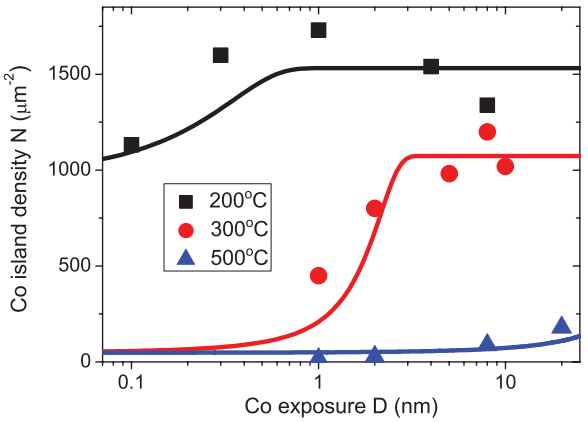

FIG. 4. (Color online) Experimental (symbols) and theoretical (curves) dependences of the island density on the Co exposure at three different temperatures.

The dependence of the invariant size on the number of atoms in the island is determined by the growth mechanism. Regardless of the growth law, the surface density of islands is obtained by integration of the size distribution in the form[24]

$$N(D) = N_{\max}[1 - \exp(-e^{c(D-D_*)})]. \tag{5}$$

Here, $N_{\max}$ is the maximum island density acquired upon the completion of nucleation stage, D_* is the critical Co exposure at which the nucleation rate reaches its maximum, and c the parameter which is inversely proportional to the size distribution width. The maximum density decreases with the temperature as the Arrhenius exponent,[23,24]

$$N_{\max} = N_0 \exp\left(\frac{E_D}{k_BT}\right). \tag{6}$$

Here, N_0 is a constant and E_D is the quantity of the order of activation energy for the surface diffusion. Since the distribution width increases due to thermal fluctuations, the c value must decrease with temperature. The fits in Fig. 4 are obtained from Eqs. (5) and (6) at $E_D = 0.055$ eV, $N_0 = 200\ \mu\text{m}^{-2}$, and $c = 5.76 - T/135$ K. The critical exposure D_* is set to zero at 200 °C, 1.6 nm at 300 °C, and 54 nm at 500 °C (we note that most of the Co atoms desorb from the surface at elevated temperatures so that these fitting values do not necessarily contradict the Volmer-Weber growth mode). It is seen that theoretical curves represent fairly well the experimental data at $T = 300$ °C and 500 °C. However, we cannot describe a slight decrease of density with D at 200 °C, which is clearly seen on the experimental dependence in Fig. 4. This effect is most probably explained by a partial coalescence of a dense ensemble of islands at lower temperatures. As follows from Fig. 4, the nucleation stage is faster at lower temperatures, having been fully completed at 1 nm exposure at 200 °C and at 3 nm exposure at 300 °C, and not yet completed after the deposition of 11 nm of Co at 500 °C.

B. Role of fluorite surface steps

Careful analysis of SEM and AFM images reveals that the spatial distribution of Co islands on the CaF_2 surface is highly influenced by the fluorite surface steps. For a migrating adatom, the probability to be trapped at a surface step is usually

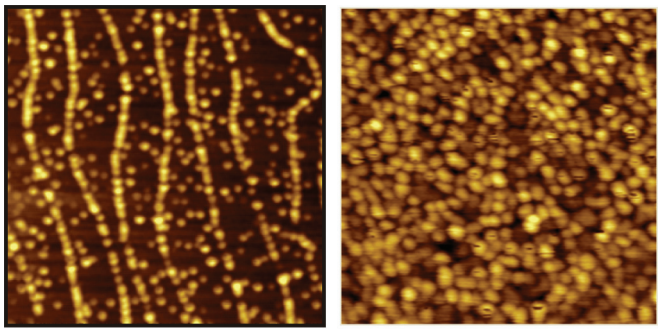

(a) (b)

FIG. 5. (Color online) AFM images of Co islands at 100 °C after deposition of 1 nm (a) and 8 nm (b) of Co. The image size is 620 nm × 620 nm × 9 nm.

higher than on a terrace because the step sites have more dangling bonds. Nucleation therefore occurs at the step much more often, provided that the adatom diffusion length is large enough to reach the step and its kinetic energy is low enough to feel the difference between the at-the-step and on-the-terrace bonding energies.[25] It has been found in the present work that Co nucleation starts at CaF_2 steps in the entire temperature range studied (100 °C–600 °C). This is most clearly seen at temperatures below 300 °C, where the distance between the neighboring Co islands is much less than the width of CaF_2 terraces at the initial growth stage. Below 1 nm of Co deposited, the islands tend to form chains along the steps, with a smaller fraction of on-the-terrace islands [Fig. 5(a)]. As the exposure increases, more islands emerge on the terraces so that the island distribution transforms to one that is spatially uniform, as shown in Fig. 5(b).

In order to better understand the growth mechanisms of Co islands, the height distributions were obtained from the statistical analysis of AFM images of the samples grown at different temperatures and deposition times. Typical height histograms at 100 °C (2 nm of Co deposited) and 300 °C (20 nm of Co deposited) are shown in Fig. 6. Different T and D are chosen in order to more clearly demonstrate the difference in the distribution shapes. To model the experimentally observed height distributions, we use the universal double exponential distribution over invariant sizes ρ (Refs. 22–25):

$$g(\rho,z) = cN_{\max} \exp[c\,(z-\rho) - e^{c(z-\rho)}]. \tag{7}$$

Here, $z(t)$ is the time-dependent most representative size (which equals the mean size in the Gaussian approximation) and c is the same constant as in Eq. (5). As discussed in Refs. 1,22–24, and above, when the island is primarily fed by the direct impingement to its surface, its growth rate di/dt is proportional to $H^2 \propto i^{2/3}$, as given by Eq. (1). For the island growth by random surface diffusion with small diffusion length compared to a typical island size, the growth rate is proportional to the island base perimeter, i.e., $di/dt \propto H \propto i^{1/3}$. When the island growth is induced by the diffusion along the surface step (the step diffusion), the growth rate di/dt is size independent. We can therefore write down quite generally

$$di/dt \propto H^n, \tag{8}$$

with $n = 0$, 1, 2 for the growth by the step diffusion, surface diffusion, and direct impingement, respectively. Since the island growth rate in terms of invariant size, $d\rho/dt$, should be H independent,[5,22–24] we obtain

$$\rho \propto H^k, \tag{9}$$

with $k = 3 - n = 3$, 2, 1 for growths by the step diffusion, surface diffusion, and direct impingement, respectively.

Distributions expressed in terms of different size-related variables should preserve the number of islands,[22] yielding $f(H,t)dH = g(\rho,t)d\rho$. Therefore, Eqs. (7) and (9) yield the height distributions of the form

$$f(H,t) = A_k H^{k-1} \exp\left\{c_k\left[H_0^k(t) - H^k\right] - e^{c_k[H_0^k(t)-H^k]}\right\}. \tag{10}$$

Here, A_k are the normalization constants, c_k are the coefficients that determine the distribution width, and $H_0(t)$ is the time-dependent most representative height relating to the distribution maximum. The dependences given by Eq. (10) are shown by lines in Fig. 6 at different k and the fitting parameters

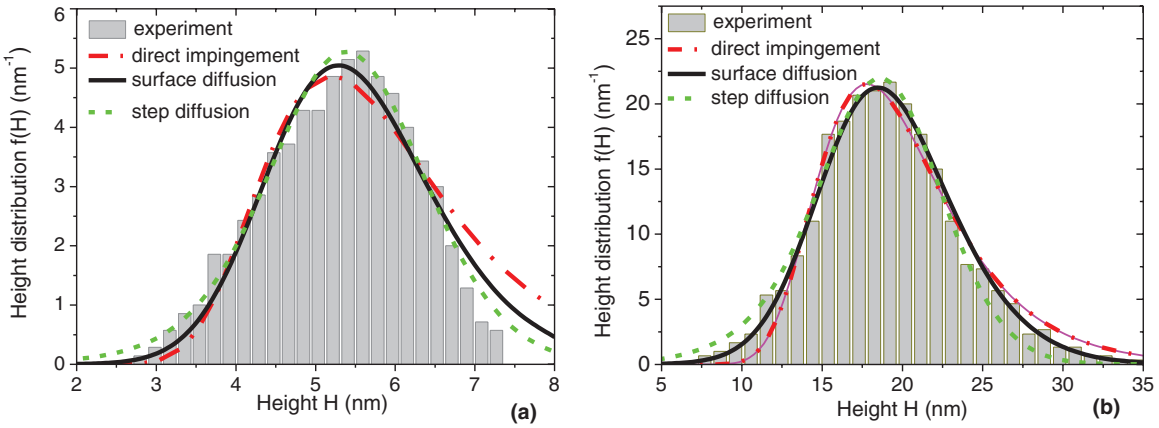

FIG. 6. (Color online) Experimental height distributions of Co islands at T =100 °C, D = 2 nm (a) and T =300 °C, D = 20 nm (b), fitted by different distributions with the following parameters [index (1) direct impingement, (2) surface diffusion, (3) step diffusion]: $A_1 = 13.2$, $c_1 = 0.91$, $H_0^1 = 5.2$ nm, $A_2 = 2.64$, $c_2 = 0.1$, $H_0^2 = 26$ nm, $A_3 = 0.53$, $c_3 = 0.0132$, $H_0^3 = 125$ nm in (a); and $A_1 = 58.5$, $c_1 = 0.258$, $H_0^1 = 17.8$ nm, $A_2 = 3.25$, $c_2 = 0.0071$, $H_0^2 = 308$ nm, $A_3 = 0.19$, $c_3 = 0.000\,29$, $H_0^3 = 4700$ nm in (b).

listed in the figure caption. It is seen that the experimental histogram at 100 °C is best fitted with the step diffusion mode. The histogram at an intermediate growth temperature of 300 °C is little better fitted by the two-dimensional ballistic diffusion model, which seems reasonable because the Co exposure is ten times larger and the islands are much bigger than after the deposition of 2 nm of Co at 100 °C. However, a combination of contributions from different growth mechanisms is not excluded in this case.

There have been relatively few experimental studies of the influence of surface steps on the formation and growth of metallic nanoparticles. In Ref. 26, it has been found that at-the-step nucleation of Au islands suppresses the epitaxial growth on the KBr terraces and gives rise to the formation of multiply twinned particles. As revealed by the scanning tunneling microscopy studies of Au growth on the MgO(100) surface,[5] the nucleation of Au islands at the surface steps becomes effective only under special growth conditions, while on-the-terrace nucleation always remains dominant. Interestingly, it has been shown that a reduced density of Au particles near the surface steps can be observed under certain conditions. This effect was related to the reduced concentration of Au adatoms due to their rapid capture by islands growing at the step edges. Opposite to this observation, Fig. 5(a) clearly shows a much higher linear density of Co nanoparticles at the step edges compared to any direction on the terraces. We note that the nucleation of Co nanoparticles on CaF_2 may not be completely random but occurs with a higher probability at the surface defects, as often observed for other metals on insulating surfaces.[27] In particular, an important role of at-the-step nucleation was revealed by the STM study of the influence of surface defects on the growth of Pd nanoparticles on TiO_2(110).[28] It was also found that the cyclic annealing of Pd islands at 672 K resulted in the increase of their size with simultaneous reduction of the surface density, especially on the terraces. However, a certain amount of Pd particles remained on the terraces, most likely due to coalescence of smaller islands before they reached the step edges. In the following section, we will show how on-the-terrace nucleation can be completely suppressed in our material system by applying a modified growth procedure.

C. Growth with low-temperature seeding layer

We now consider the influence of a low-temperature seeding layer on the resulting morphology of Co islands. As discussed above, a weak sticking of Co to the CaF_2 surface suppresses its nucleation and growth at elevated temperatures (above 300 °C), where most of the material is lost because of incomplete condensation. On the other hand, high-temperature growth is believed to significantly improve the crystal quality of Co islands. Furthermore, the growth well above the hcp-to-fcc crystallographic transition temperature for Co [450 °C (Ref. 29)] should favor single-crystalline fcc lattice. Another challenge is to produce densely packed linear chains of high-temperature islands aligned along the surface steps. This is difficult because of a large diffusion length at intermediate temperatures, where the distance between the neighboring nucleation sites at the same step becomes comparable to the step spacing. A 0.02–0.5-nm seeding layer of Co was therefore grown on CaF_2 at a low temperature (from room temperature up to 200 °C) prior to the high-temperature Co deposition at 300 °C–700 °C. It has been found that the two-step growth procedure enables the fabrication of perfectly aligned islands decorating the steps, with the density being much higher and the size much larger than in the case of single-stage high-temperature growth. These features are clearly seen from comparing the morphologies shown in Figs. 5(a) and 7(a). The sample obtained by the two-step procedure contains much less on-the-terrace islands between the chains, while its better crystallinity is confirmed by RHEED. As the Co exposure increases from 13 to 30 nm, the islands get larger and the spatial ordering is lost [Fig. 7(b)]. As seen from Fig. 7(b) after 30 nm exposure and Fig. 7(c) after 45 nm exposure, the coalescence process leads to a significant decrease of Co island density.

The influence of growth conditions on the resulting morphology of Co nanoislands in the two-step approach has also been studied. We have found that the optimal exposure of the low-temperature seeding layer is between 0.02 and 0.5 nm. Below 0.02 nm, the seeding layer becomes ineffective because the islands nucleate too far from each other. Above 0.5 nm, the crystal quality of the high-temperature Co layer is impeded as revealed by RHEED. It has been found that the efficient

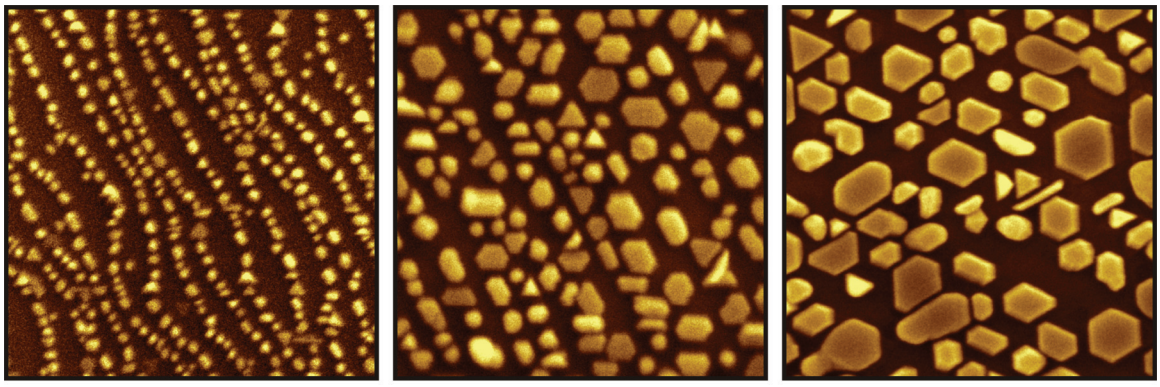

FIG. 7. (Color online) SEM images of Co islands grown with a 0.1-nm seeding layer and various exposures at the main stage: (a) 13 nm, (b) 30 nm, (c) 45 nm. The image size is 1000 nm × 1000 nm.

suppression of on-the-terrace nucleation takes place only when the growth temperature at the second stage is between 500 °C and 700 °C. At lower temperatures, the on-the-terrace to at-the-step density ratio increases drastically while at higher temperatures the CaF_2 buffer layer is no longer stable.

The suppression of on-the-terrace nucleation at elevated temperatures can be qualitatively explained by the exponentially decreasing temperature dependences of on-the-terrace nucleation rate and surface density,[24] as given by Eq. (6). Indeed, small on-the-terrace Co islands nucleated at the low-temperature step may either decompose to adatoms or migrate as a whole toward much more stable at-the-step islands when the surface temperature is increased. After that, no new islands nucleate between the steps. Rather, a certain percentage of deposited Co diffuses toward at-the-step islands and contributes to their growth while the rest of the Co reevaporates. This scenario is somewhat similar to the behavior of Pd atoms on the $TiO_2(110)$ surface under the cycling annealing.[28] However, the preferential island location at the steps is much better pronounced in our case.

The total area covered by the islands gradually increases with the cobalt exposure from ∼8% for a 5-nm sample to ∼54% for the 45-nm sample shown in Fig. 7(c). Reaching a continuous Co coverage of the surface thus requires a long exposition time, where the coalescence of islands should be taken into account. As for the coalescence mode, a high surface mobility of Co at elevated temperatures does not seem to favor the solidlike coalescence. This is clearly seen from Fig. 7: If the coalescence had a solidlike character, the linear chains of islands with small interisland distance in Fig. 7(a) would have been soon transformed into continuous stripes that are not present in Fig. 7(b). Instead, the islands get larger in size simultaneously with the gaps between them. This effect is most probably due to an interdiffusion of adatoms along the island surfaces and bases, a process that tends to decrease the base perimeter after two or more islands merge. The difference between the solidlike coalescence at low temperatures and the liquidlike coalescence at high temperatures is illustrated in Fig. 8. The complex coalescence process shown in Fig. 8(b) requires additional study. In any case, it is not of the Kolmogorov type.[30] Indeed, the solidlike coalescence is described by the Kolmogorov formula for coverage $\sigma(t)$:[30]

$$\sigma(t) = 1 - \exp(-\lambda D^{\beta}), \tag{11}$$

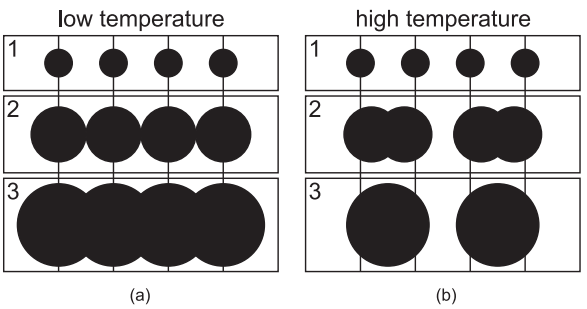

FIG. 8. Schematics of the solidlike coalescence at low temperatures (a) and the liquidlike coalescence at high temperatures (b).

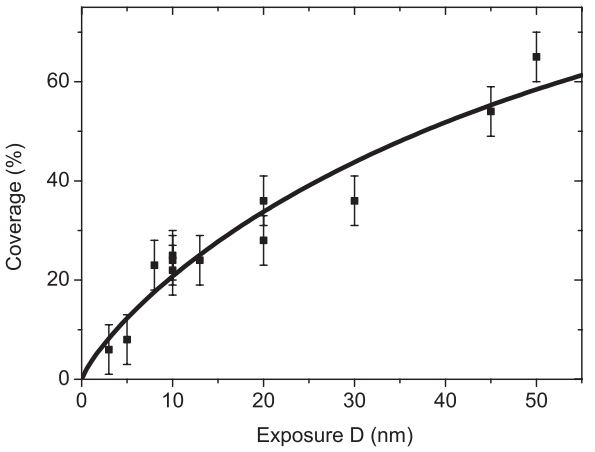

FIG. 9. Co coverage as a function of the exposure (symbols), fitted with the Kolmogorov exponent with $\beta = 0.825$.

where the index $\beta = 2/3$ for the step diffusion growth, 1 for the surface diffusion growth, and 2 for the growth induced by the direct impingement (the latter scenario is supported by the measured linear height-exposure dependence). The best fit to the experimental data on the Co coverage as a function of the exposure shown in Fig. 9 is obtained at $\beta = 0.825$ with $\lambda = 0.0348\ \text{nm}^{-0.825}$. Such a large discrepancy with the Kolmogorov values of β shows again that the coalescence process is not of the solidlike type.

IV. CRYSTAL STRUCTURE, EPITAXIAL RELATIONS, AND DEFECTS OF Co NANOPARTICLES

It is well known that Co has the hcp crystal structure with ABABAB··· stacking sequence under bulk form at room temperature, which transforms into the fcc structure with ABCABC··· stacking above 450 °C.[29] In strained thin films and particularly in nanostructures such as nanowires[31,32] and nanoneedles,[33] metastable crystal phases are observed quite often. In the case of Co, stabilization of the fcc metastable phase has been observed in ultrathin Co films on Pt(111),[34] arrays of Co epitaxial nanoparticles on Cu(110),[35] Co thin films on vicinal Au(233),[36] Co thin films on NiO(111),[6] and Co nanocrystals on $SrTiO_3$(001)-2 × 2.[7] The strained body centered cubic (bcc) phase has been revealed in Co pseudomorphic layers on Pt(001) and in a number of other systems.[37] More exotic Co crystal phases have also been found under certain conditions. In particular, the double hcp (dhcp) phase[38] with ABACABAC··· stacking sequence was obtained at high temperatures and pressures, while a complex cubic phase (of the β-Mn type) with the unit cell consisting of 20 Co atoms[39–41] was found in chemically prepared Co nanoparticles. Given this variety of possible structures, we have performed a detailed analysis of the crystal phase of our Co nanoislands obtained at different growth conditions.

A. RHEED data and analysis

The crystal structure of Co nanoparticles was first examined by RHEED during and after growth. Typical diffraction patterns from the samples grown at 100 °C, 300 °C, and 500 °C are presented in Fig. 10. The contrast and brightness of

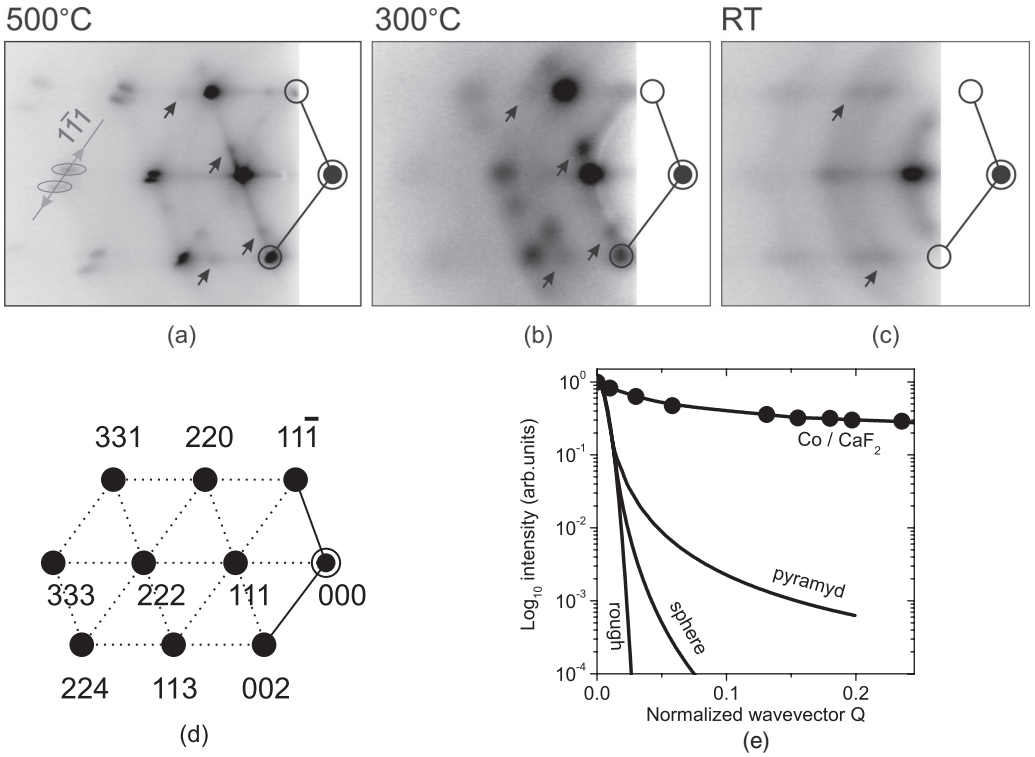

FIG. 10. RHEED patterns from Co islands grown at 500 °C (a), 300 °C (b), and 100 °C (c). (d) fcc reciprocal lattice nodes in [1-10] zone. (e) Experimental (1-11) profile through (333) reflection for the 500 °C sample, compared to the calculated streak profiles for 20-nm crystals of different shapes. The wave vector Q is normalized to the length of Co[111] reciprocal space vector.

the diffraction spots show that the crystal quality improves with increasing the growth temperature. The best ordered and brightest spots are obtained at 500 °C–600 °C [Fig. 10(a)]. The spots are identified as originating from the fcc lattice co-oriented with the underlying CaF_2 layer [Fig. 10(d)]. Traces of fcc lattices rotated by 180° around ⟨111⟩ axes are also present (indicated by the black arrows). At lower temperatures between 200 °C and 300 °C, the fcc structure is less distinct [Fig. 10(b)]. In addition to the dominant fcc pattern, a few rotational twins corresponding to 180° rotations around four ⟨111⟩ axes are recognized (indicated by the black arrows). In the temperature window between room temperature and 100 °C, the diffraction patterns show polycrystalline arcs and low-contrast fuzzy spots. The latter may still be identified as belonging to the fcc phase [Fig. 10(c)].

Interestingly, the RHEED patterns of the 500 °C sample exhibit bright Co streaks: The [111] streaks show up as horizontal lines perpendicular to the surface, while the [11-1] streaks are seen as the 70.5° inclined lines. The position of these lines is independent of the incident angle, which rules out any connection with the Kikuchi lines. Since the (111) surface has a threefold symmetry, two more streaks are expected: the [1-11] and [-111] ones lying out of the depicted [1-10] zone. The presence of these two streaks contributes to the Bragg reflection splitting which is well pronounced in Fig. 10(a). When the sample is rocked away from the diffraction position for a given reflection, this reflection splits into two bright spots that move apart parallel to the [001] axis, as shown by arrows in Fig. 10(a). These spots are intersections of the [1-11] and [-111] streaks with the Ewald sphere. The upper curve in Fig. 10(e) shows the intensity profile measured along such a streak passing through the (333) reflection in the [1-11] direction. The profile was recorded by changing the incident angle and plotting the spot intensity against its position.

To explain the observed streaking, we note that the RHEED streaks usually appear when the diffracting volume has a finite size along the streak either because of the finite size of the sample (e.g., a thin layer) or because of a small penetration depth of the incident radiation (e.g., at grazing incidence to a flat surface due to the total external reflection). Streaking is also known to occur on nonflat grooved-and-ridged surfaces,[42] where the electron beam propagates along the grooves and produces inclined streaks perpendicular to the groove walls. In the case of isolated $Co/CaF_2(111)$ islands, electrons penetrate through the entire island volume even at grazing incidence. For 10–20-nm size islands, only some 50–100 atomic planes get illuminated, which results in the reflection widening of the order of 0.01–0.02 reciprocal lattice units. These values are much smaller than the observed streak length. In addition to the size-related widening (which should be almost isotropic for our islands), the anisotropic facet-related widening may occur perpendicular to the facet.[43] The facet streaks propagate beyond the size-defined reflection width and fade away as Q^{-2}. In the region where the facet streak becomes separated from the reflection core, its intensity decreases by several orders of magnitude and falls out of the detector dynamic range if measured on the same brightness scale as the main reflection. To illustrate the size-related and facet-related reflection widening, Fig. 10(e) shows the calculated intensity

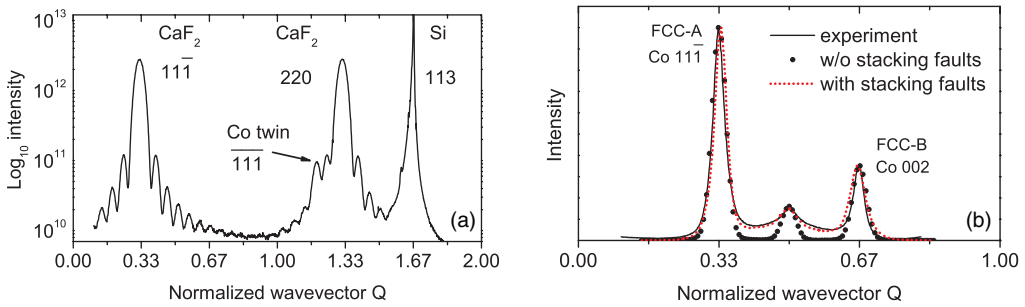

FIG. 11. (Color online) XRD profiles passing perpendicular to the sample surface through CaF_2 (11-1) and CaF_2 (220) reflections (a), and through Co(11-1) and Co(220) reflections (b) for the sample grown at $T = 500\,^{\circ}$C with $D = 15$ nm by the one-step procedure. The simulation profiles (with and without stacking faults) are shown in (b). The wave vector Q is normalized to the length of reciprocal space vector of CaF_2 [111] in (a) and of Co[111] in (b).

profiles for 100-monolayer (ML) islands of various shapes: a pyramid, a sphere, and a rough surface object without any defined shape. All the profiles have the same value of FWHM but decay differently at higher Q. The fastest intensity decay is observed for a rough surface, the isotropic Q^{-4} decay is typical for a sphere, while the Q^{-2} facet streaks are present for a pyramid. Comparing the calculated profiles with the experimental one, it is clear that the bright long streaks in our RHEED patterns are related neither to the size nor to the shape of the Co islands.

Another reason for streaking is the variation of lattice constant in the streak direction.[44] These streaks, however, are also short compared to the inter-reflection distance, because the variation of lattice constant can hardly exceed a few percent. Furthermore, the strain-induced reflection widening should increase with the reflection order, which is clearly not the case in our diffraction patterns.

Finally, streaks may be due to the presence of planar defects perpendicular to the streak direction, in particular, stacking faults in the fcc lattice. The streak length in this case should be defined by the correlation length of the faulted structure. Antiphase boundaries may naturally occur in the fcc lattice of Co, especially considering that bulk Co has the hcp lattice structure. The fcc lattice consists of an ABCABCABC$\cdots$ sequence of close packed (111) planes, where A, B, and C denote the planes with three different lateral shifts. The hcp lattice has an ABABAB$\cdots$ stacking sequence with just two types of shifts. One may expect that stacking faults are inserted into the stacking sequence during the growth or cooldown process. As follows from numerical calculations presented in the next section, a random insertion of the faults parallel to the sample surface indeed results in the appearance of the (111) streaks normal to the surface. This can be extrapolated to a situation where the stacking faults exist in each $\langle 111 \rangle$ direction producing four streaks similar to those observed in the diffraction patterns from our Co islands.

It has been found that streaking is especially pronounced for the islands grown at high temperature, most probably because the lattice contraction after cooling from 500 °C–600 °C to room temperature is considerable and because big islands are better bound to the underlying CaF_2 layer. Insertion of stacking faults could be the way to release strain induced by thermal contraction. Islands grown at 100 °C–300 °C are much smaller and therefore are less tightly bound to the CaF_2 layer. They may contract as a whole without introducing any stacking faults. This explains why no streaks are observed in the RHEED patterns from low-temperature Co islands.

B. X-ray diffraction

To obtain more precise information about the crystal structure, x-ray diffraction from the high-temperature samples (10–20 nm of Co exposure) was measured using the synchrotron radiation. The experiments were conducted in the following sequence. Several long-range profiles of the scattered intensity distribution (normal to the substrate and passing through the CaF_2, Si, and Co off-specular reflections) were first measured to get a sketch of the reciprocal lattice and to determine epitaxial relations. The Bragg reflections were then measured with high accuracy to determine the Co lattice constants. The Co lattice in nanoparticles was found to be fully relaxed, with the lattice constant being equal to its bulk value: $a = 3.544$ Å. The 3D mapping carried out in different cobalt Bragg positions confirmed that {111} streaks passing through the Co reflections are indeed present as was previously observed by RHEED.

Figure 11(a) shows the scattered intensity profiles passing through the CaF_2(11-1), CaF_2(220), and Si (113). The presence of these three reflections on the same streak confirms that the CaF_2 lattice is rotated by 180° around the surface normal with respect to the Si lattice. Distinct thickness oscillations around CaF_2 reflections confirm the high quality and flatness of the CaF_2 layer. The period of oscillation corresponds to the CaF_2 buffer layer thickness of 19 ML. A small extra peak at $Q = 1.19$ is due to a slightly off-streak Co (-1-1-1) reflection originating from one of the twinned fcc lattices of Co.

Figure 11(b) shows the profile passing through the Co(11-1) reflection, measured normal to the surface. The profile contains three peaks that cannot be ascribed to a single-crystalline fcc or hcp stacking sequence. The dominating peak is the Co (11-1) peak at $Q = \frac{1}{3}$, which is characteristic of the fcc lattice which is co-oriented with CaF_2 (type-A epitaxial relation). The smaller peak at $Q = \frac{2}{3}$ is most likely the Co(002) peak originating from the fcc type-B lattice, rotated by 180° around the substrate normal. The smallest peak at $Q = \frac{1}{2}$ corresponds to the Co(-1101) plane belonging to the hcp phase with the c axis parallel to the CaF_2 [111] axis. In the first approximation, we assume that the observed profile is a linear combination of these three peaks, i.e., each island is single crystalline and has

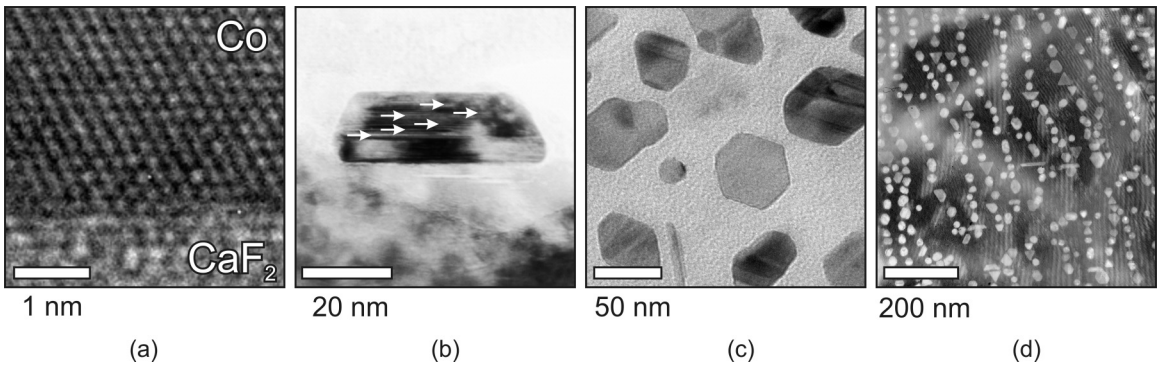

FIG. 12. TEM images of Co islands on the CaF_2 surface: Cross-section views showing the Co/CaF_2 interface region (a) and a single Co island (b); in-plane views of the Co/CaF_2 samples with the Co exposure of 20 nm (c) and 10 nm (d).

either fcc-A, fcc-B, or hcp lattice. Such a model was used to simulate the XRD profile in the kinematic approach. By adjusting the amount of Co (∼18 MLs) and the percentage of fcc-A, fcc-B, and hcp phases (60%, 22%, and 18%, respectively), it was possible to fit the peak positions, heights, and widths [the dotted curve in Fig. 11(b)]. The fit is, however, not satisfactory, because the adjusted island height of 18 MLs (∼3.6 nm) is four to five times smaller than that measured by AFM. Furthermore, the experimental curve contains a streaklike region extending from $Q = 0.33$ to $Q = 0.67$, while the theoretical curve rapidly drops to zero between the reflections. We can thus conclude that the streaks propagating in ⟨111⟩ directions are too bright and too long to be attributed to facets. More likely, they are associated with stacking faults as discussed in Sec. IV A.

We therefore considered a more complex model assuming that the three stacking orders coexist within a single Co island that interacts coherently with the incoming x rays. The Monte Carlo simulation involved random insertion of stacking faults and averaging over a few thousands of islands. Atoms within a given island scatter coherently, while different islands are incoherent with respect to each other. The percentage and the domain size of each stacking order were used as fitting parameters. The best fit [shown by the dash-dot curve in Fig. 11(b)] is obtained for 49% of the fcc-A phase with the domain size of eight layers, 36% of the fcc-B phase with the same domain size, and 15% of the hcp phase with the domain size of six to eight layers. It should be noted that the obtained fcc-A to fcc-B ratio is rather high for this particular sample. Samples grown with the seeding layer usually contain a much higher percentage of the fcc-A phase. In any case, our XRD data illustrate well the general conclusion: Accounting for stacking faults is absolutely necessary for the correct description of Co crystal structure.

Somewhat similar phase mixing was reported earlier in Ref. 34 where the Co islands were grown on the Pt(111) substrate. The measured XRD profiles contained the dominant peak at $Q = 0.5$ and two smaller peaks of equal intensity at $Q = 0.33$ and 0.67. These peaks were attributed to a linear combination of fcc-A, fcc-B, and hcp stacking orders with a considerable fraction of disordered phase. In our XRD analysis, we are able to describe fairly well the observed XRD profiles within a statistical model of stacking faults without introduction of any disordered state.

C. Electron microscopy

Several samples with Co nanoparticles were also studied by TEM and HRTEM. Figure 12(a) shows the Co/CaF_2 interface region for the sample grown at 100 °C. It is seen that the interface is abrupt and the structure is locally defect free. As for the stacking faults discussed in the previous sections, the faults parallel to the interface are seen as horizontal lines (indicated by arrows) in Fig. 12(b) which shows a typical cross-view TEM image of a single island. Stacking faults inclined to the interface are also seen in the in-plane image of Co islands grown with a seeding layer and 20 nm Co exposure [Fig. 12(c)].

Since Co islands nucleate on a CaF_2 surface whose lattice constant is 1.5 times larger, different epitaxial registry at the interface is possible. The simplest alignment corresponds to the case where every third Co atom occupies the same site on the CaF_2 surface. Shifting the Co lattice as a whole to the adjacent CaF_2 site would result in the identical Co/CaF_2 interface structure. However, the Co lattice in the first alignment will be phase shifted with respect to the second one. Whenever the neighboring islands emerge with different lattice registry as described above, an antiphase boundary naturally forms upon coalescence of these islands.

Figure 12(d) shows the TEM image of the sample grown with 10 nm Co exposure by the two-step growth procedure with a seeding layer. It is seen again that the islands are aligned in linear chains along the CaF_2 surface steps in this case. Comparing the samples with 20 and 10 nm Co exposure, one can conclude that most islands have a hexagonal shape. At a lower coverage, however, a smaller fraction of triangular islands is present. Since the island shape is of particular importance for the resulting properties, the next section will address this problem in more detail.

V. SHAPE OF Co NANOPARTICLES

SEM studies were carried out for a sample grown with a seeding layer, 45 nm Co exposure at a temperature of 600 °C. A typical plan view SEM image [(Fig. 13(a)] shows that the majority of the islands have a hexagonal cross section. Hexagonal islands are oriented in the same way, with the sides directed at 120° to each other and parallel to the Si ⟨110⟩ directions. To obtain the three-dimensional island shape, higher magnification images were taken for the sample inclined by 45° and 70° off-normal toward the CaF_2 [-211]

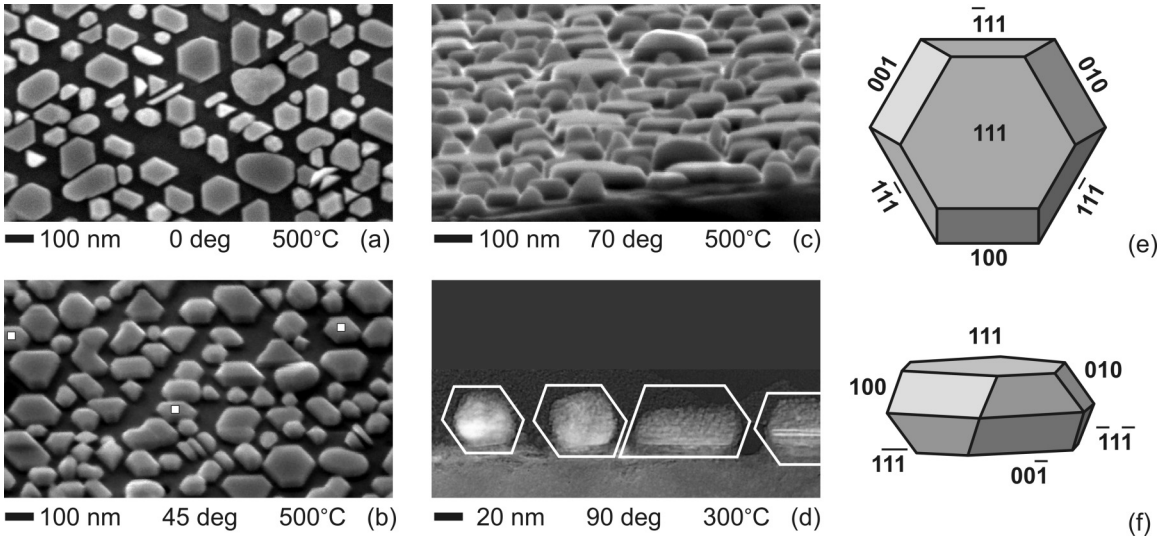

FIG. 13. SEM (a)–(c) and TEM (d) images of Co islands viewed at different angles to the surface. Schematic illustrations of the island geometry are shown in (e) and (f).

[Figs. 13(b) and 13(c), respectively]. Most islands have a hexagonal flat top that should correspond to the Co(111) plane. It is also seen that the islands are faceted from six sides. Three facets have a rectangular shape and are identified as the Co{100} facets, while the other three have a trapezium shape and are identified as the Co{111} facets. The schematic illustration of the geometry is shown in Figs. 13(e) and 13(f). This shape is in agreement with the data of Ref. 7, where the faceting of Co islands with the {111} and {100} planes was also observed. The orientation of the faceted islands with respect to the CaF_2 crystallographic directions agrees well with our RHEED data and confirms that the lattices of Co and CaF_2 are co-oriented. A few islands terminated by the same facets but rotated by 180° are also found on the SEM images [indicated by white squares in Fig. 13(b)]. The number of rotated islands is approximately three times smaller than of the nonrotated ones. This ratio gives the twinning probability which is also in agreement with the RHEED and XRD data presented in the previous section.

To measure the angles between the facets and the (111) plane, a number of TEM cross-views [perpendicular to the substrate surface and parallel to the CaF_2 (1-10) plane] have been analyzed. Similar types of the island shape were revealed in the growth temperature range between 100 °C and 500 °C. A typical example of the cross sections (for a single-stage 300 °C sample in this particular case) is shown in Fig. 13(d). The Co islands are seen as polygons with sharp edges, the shapes shown by white lines in the figure. The horizontal lines correspond to the Co(111) planes, the lines directed at a 70.53° angle to the interface are the (11-1) planes, and the 54.74° inclined lines are the (001) planes. The intensity variations seen as horizontal lines correspond to the (111) stacking faults. Quite interestingly, the TEM images show that many islands are of a double-trapezium cross section; i.e., they have narrower tops and bases but are considerably wider in the middle part. While island tapering in the growth direction looks natural during epitaxial growth, the reverse tapering is less frequent. One of the explanations of the reverse tapering might be the minimization of the total surface area in heteroepitaxy. Indeed, the surface energy of $CaF_2(111)$ is considerably lower compared to the energy of any of the Co facets. The formation of a heterogeneous Co/CaF_2 interface might also be energetically costly. Therefore, the energetically preferred shape might favor the minimization of the Co/CaF_2 interface area, reflecting the preferential nonwetting configuration of Co on CaF_2 at high enough temperatures. Another reason for decreasing the island base area is a weak Co/CaF_2 sticking. The sticking should be especially weak at the edges of the island base where Co is bonded to both Co and CaF_2. These atoms can be easily removed from their sites during growth, leading to the reverse tapering.

VI. MAGNETIC AND MAGNETO-OPTICAL PROPERTIES OF Co NANOPARTICLES

As discussed in the previous sections, the density, size, shape, and spatial distribution of Co islands on CaF_2 (111) can be tuned by the growth conditions such as temperature, cobalt exposure, and the initial structure of the fluorite surface. Let us now see how the morphology affects the magnetic and magneto-optical properties of these structures. We first evaluated the magnetic moments of Co atoms in three samples grown with the same cobalt exposure of 20 nm but at different temperatures of 100 °C, 300 °C, and 500 °C (see Fig. 2). The surface density of Co atoms (N_{Co}) was measured by applying the MEIS method. Total magnetizations (M) were obtained by SQUID measurements at room temperature. The results are summarized in Table I. It is seen that both N_{Co} and M values strongly decrease with temperature. The value of the atomic magnetic moment ($m = M_{Co}/N$) for the 100 °C sample is $1.0\mu_B$, which is noticeably less than the calculated bulk value $\sim 1.6\mu_B$ for fcc Co structure.[45] The reduced values observed in our experiments can be caused by several reasons: decrease of T_c in nanoparticles with respect to a continuous magnetic layer, a partial oxidation of Co nanoparticles, which is quite

TABLE I. Surface density of Co atoms N_{Co}, total magnetization M, and atomic magnetic moment m in Co island grown at different temperatures.

Growth temperature (°C)	N (10^{15} atom/cm^2)	M (10^{-5} emu/cm^2)	m (μ_B)
100	162	155	1.0
300	84	64	0.8
500	13	5.9	0.5

likely, and possible formation of cobalt fluoride at elevated temperatures.

It has been found that the magneto-optical effects in our structures also strongly depend on the growth conditions used. In particular, Fig. 14 shows the magnetic field dependence of the polar (PMOKE) and longitudinal (LMOKE) magneto-optical Kerr effect in the structures grown at a fixed temperature of 100 °C and different Co exposures: $D = 3$, 5, and 8 nm. It is seen that the amplitudes of both polar and longitudinal MOKE decrease drastically with the decrease of Co exposure. This correlates with the measured total magnetization of these structures obtained by SQUID. LMOKE exhibits a well-pronounced hysteretic behavior. In contrast, PMOKE exhibits a nonhysteretic dependence on the magnetic field. This indicates that the magnetization at $H = 0$ is in-plane oriented so that applying a surface normal magnetic field H results in an out-of-plane rotation of the magnetization.

The change of sign of both PMOKE and LMOKE in the structures with isolated magnetic nanoparticles has been observed earlier for different magnetic particles and substrates. The effect was ascribed to the light scattering from nanoparticles combined with the reflection from the substrate.[46,47] We have also found that the decrease of the surface density of Co islands and the change of their volume (e.g., with increasing the growth temperature) strongly affects the out-of-plane magnetic anisotropy. Figure 15 shows the magnetic field dependence of PMOKE, normalized to the PMOKE magnitude at $H = 20$ kOe. The measured structures were grown at fixed $D = 8$ nm and different temperatures. It is expected that the out-of-plane magnetic anisotropy is determined by the

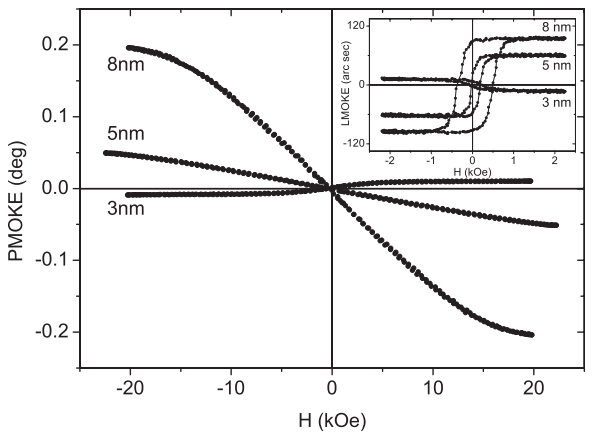

FIG. 14. Magnetic field dependence of PMOKE in structures grown at 100 °C and different Co exposures $D = 3$, 5, and 8 nm, the inset showing the hysteresis loops measured by LMOKE.

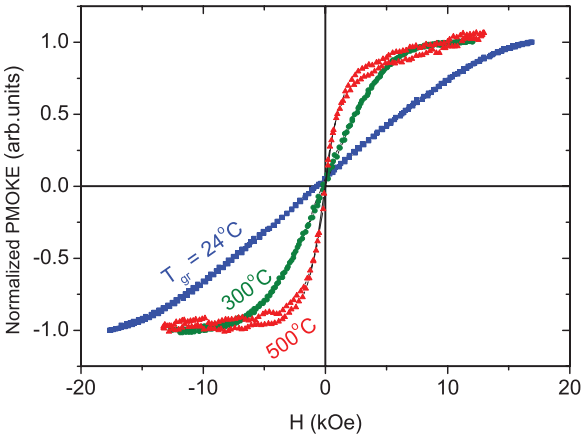

FIG. 15. (Color online) Magnetic field dependence of the normalized PMOKE for the structures with $D = 8$ nm grown at RT, 300 °C, and 500 °C.

shape anisotropy, the magnetocrystalline anisotropy, and the anisotropy induced by the deposit-substrate interactions. In the structures grown at room temperature and 100 °C, the Co coverage of the substrate is large so that the magnetic layer is a two-dimensional array of interacting nanoislands. In this case, the saturation of PMOKE occurs at $H_s \cong 20$ kOe, which is close to the observed saturation value for the Co films of ~ 1 μm thickness (not shown).

In this case, the saturation field H_s for the out-of-plane orientation of the magnetic field is determined mainly by the depolarizing field $H_d = 4\pi M_s$, which is about 18 kOe in bulk Co. As discussed in Sec. III A, the increase of temperature always results in the reduced island density N (see Fig. 4). Therefore, high-temperature magnetic layers consist of magnetically isolated nanoparticles. The distance between the island centers equals ~100 nm at 500 °C, ~50 nm at 300 °C, and ~30 nm at room temperature. This leads to the decrease of H_s and the corresponding increase of the slope in the magnetic field dependence of the normalized PMOKE.

It is clear that the transformation of the magnetic layer from an array of dense particles to a dilute ensemble of weakly interacting islands should be followed by the corresponding change of the magnetic field behaviors of magnetization and PMOKE. In a dense array, the shape anisotropy can be well described by the thin-film approximation ($H_d = 4\pi M_s$), which only weakly depends on the particle shape. In a dilute ensemble of magnetically isolated nanoparticles, the anisotropy is determined mainly by the island shape and should be much smaller. This results in the corresponding decrease of the saturation field and the increase of the slope of $M(H)$ dependence at $H = 0$. It is expected that the relative contributions of the magnetocrystalline anisotropy and the induced anisotropy are approximately the same in both cases, because dense and dilute samples consist of particles of the same crystal structure, orientation, and lattice parameters. In the case of intermediate coverage, the magnetodipole interaction can also contribute to the resulting out-of-plane anisotropy.

No considerable in-plane anisotropy is expected in dense arrays similar to that shown in Fig. 5(b). The coercive field H_c in such structures should not vary with the orientation of

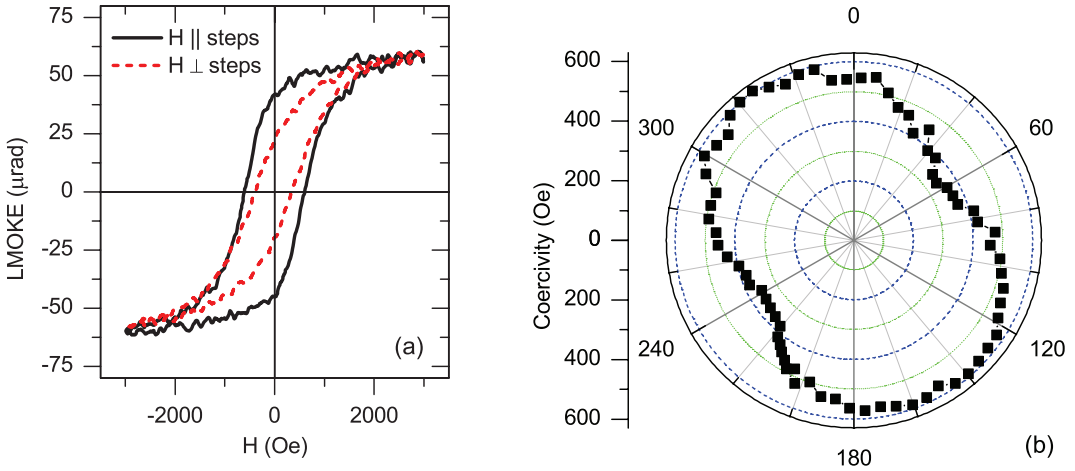

FIG. 16. (Color online) Hysteresis loop anisotropy in the sample with $D = 13$ nm, whose morphology is shown in Fig. 7(a): (a) LMOKE hysteresis loops for the magnetic field aligned parallel (black solid line) and perpendicular (red dashed) to the direction of the $CaF_2(111)$ atomic steps; (b) azimuthal dependence of the coercive field.

magnetic field in the film plane. However, remarkable in-plane anisotropy was observed in structures with almost straight linear chains of Co nanoparticles decorating the atomic steps [Fig. 7(a)]. A typical dependence of the coercive field H_c on the magnetic field azimuth ϕ for different directions with respect to the CaF_2 atomic steps is shown in Fig. 16. It is seen that the coercive field reaches its maximum when the magnetic field is directed along the atomic steps ($\phi = 150^\circ$ and 330°) and is minimum for the perpendicular direction ($\phi = 60^\circ$ and 240°). Such a behavior clearly reveals the existence of easy magnetization axis directed along the atomic steps.

Thus, the absolute value and the anisotropy of the coercive field should be sensitive to the particle density in the array. Figure 17 shows the dependence of H_c and the anisotropy parameter A [defined as $A = (H_c^{\max} - H_c^{\min})/(H_c^{\max} + H_c^{\min})$] for the structures grown with different Co exposures. At relatively small (below 10 nm) and large (above 30 nm) exposures, the in-plane magnetic anisotropy is almost negligible. However, it rapidly increases toward intermediate D and reaches its maximum at $D \approx 15$ nm. Such a behavior can be explained considering that the magnetic dipole interaction is negligible in a dilute ensemble and the distribution of easy magnetization axes in the particles is random. At large D, the spatial ordering into linear chains is lost again and the magnetic isotropy is retained.

If the particles in the linear chains are magnetically separated, possible reasons for the in-plane magnetic anisotropy include the magnetic dipole interactions and the shape anisotropy. We saw earlier [see Fig. 12(d)] that most particles in chains do not show any pronounced shape anisotropy, so the dipole interaction should be central for the observed in-plane anisotropy. Indeed, the maxima of H_c and A at $D \approx 15$ nm correspond to the maximum of the ratio $d_\parallel/d_\perp$, where $d_\parallel$ and $d_\perp$ are the averaged distances between the particle boundaries along the chains and perpendicular to the chains, respectively. The dependence $d_\parallel/d_\perp$ on D was obtained from the analysis of the correlation function calculated from AFM images at different Co exposures.

To characterize the contribution of the magnetodipole interaction into the resulting magnetic properties of the samples with linear chains of Co islands, the initial magnetization (IM) curves (often called the virgin curves) were measured for a series of high-temperature samples (whose coercivity and magnetic anisotropy are shown in Fig. 17). As shown in Refs. 48 and 49 the sign and the absolute value of the

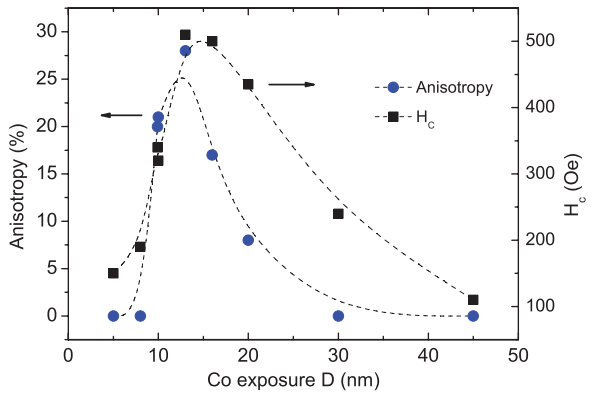

FIG. 17. (Color online) Coercive field H_c and anisotropy parameter A depending on the Co exposure D.

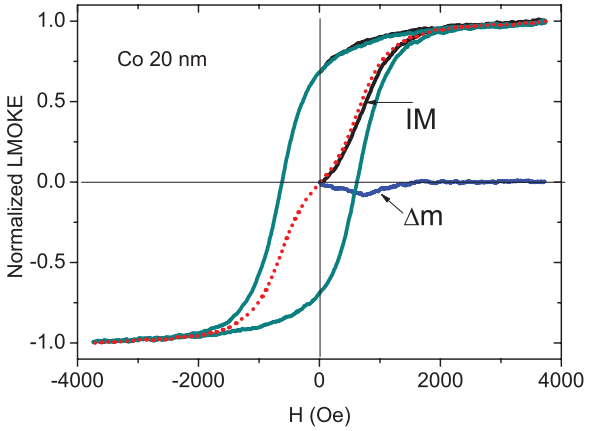

FIG. 18. (Color online) Normalized hysteresis loop, the IM, $\bar{m}$ (dotted line), and Δm curves for the sample with $D = 20$ nm.

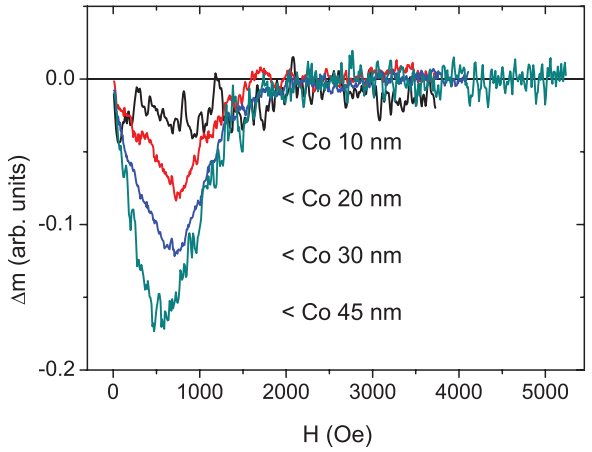

FIG. 19. (Color online) The $\Delta m(H)$ curves in the arrays with different Co exposure.

difference Δm between the IM curve and the half-sum $\bar{m}$ of the ascending and descending branches of the hysteresis loop are directly related to the type and strength of magnetic interactions in a ferromagnetic layer. This procedure is rather similar to the analysis of the Henkel plots obtained from the measurements of minor hysteresis loops;[50,51] however, it is much less time consuming. Figure 18 shows the normalized hysteresis loop (measured by LMOKE in the S polarization), the IM, $\bar{m}$, and $\Delta m = IM - \bar{m}$ curves for the sample shown in Fig. 12(c). According to Ref. 48, the negative sign of Δm reveals the dominant role of the magnetodipole interactions in the reversed magnetization of this particular array.

The Δm differences in the arrays with $D = 10$, 20, 30, and 45 nm are presented in Fig. 19. It is seen that the absolute value of Δm (which is proportional to the energy of the magnetodipole interaction) increases with the size of the nanoparticles (see Fig. 7). The magnetic anisotropy rapidly decreases for $D > 20$ nm and is almost absent in the structures with $D = 30$ and 45 nm. This is not so unexpected, because the structures with high D show no certain lateral ordering of Co nanoparticles, as seen from Fig. 7. The procedure used for measuring Δm enables the detection of the magnetodipole interaction in the sample with $D = 10$ nm, yielding the in-plane magnetic anisotropy as high as 20%. A noisier Δm curve in this sample is explained by a lower LMOKE signal due to a smaller amount of magnetic material in this structure. Interestingly, strong in-plane magnetic anisotropy of Co nanoparticles was observed earlier when corrugated CaF_2(110) layers on Si(001) substrates were used as interlayers. A grooved-and-ridged morphology of these structures considerably decreased the symmetry of the surface. This resulted in a considerable in-plane uniaxial magnetic anisotropy with the easy axis directed along the grooves.[52,53] We also note that the shapes of hysteresis curves of linearly aligned Co arrays clearly indicate the vortex formation studied earlier in a number of works; see, e.g., Refs. 54 and 55.

VII. SUMMARY

To sum up, MBE growth of Co on CaF_2/Si(111) has been studied by a number of characterization methods and modeled within the kinetic approach. The two-step procedure for growing the CaF_2 buffer on Si(111) is developed, which enables one to obtain more regular arrays of Co nanoparticles. It is shown that Co tends to nucleate at the surface steps independently of the growth temperature. When less than 1 nm of Co is deposited below 300 °C, Co islands decorate the CaF_2 surface steps. At a higher temperature and exposure, Co islands redistribute uniformly. The low sticking probability of Co onto CaF_2 results in the transition from the complete to incomplete condensation regime as the growth temperature is increased. In particular, the percentage of Co remaining at the surface is estimated as being 100% at 100 °C, 51% at 300 °C, and only 8% at 500 °C.

A series of samples were grown at different temperatures and Co exposures to gain a full understanding of the growth process and the kinetic tuning knobs that can be used for the controlled fabrication of magnetic nanoparticles. By analyzing island heights depending on the exposure, the two major growth modes are identified: the direct impingement at high temperatures and the surface diffusion at low temperatures. These results are further confirmed by analyzing the island height histograms. It is shown that both the density-exposure curves and the height distributions at different conditions are well described by the universal double exponential shapes. Theoretical curves represent fairly well the experimental data, while the fits enable the determination of some important kinetic parameters.

The crystal quality and the spatial ordering of Co islands on CaF_2 surface are shown to improve significantly when a seeding layer of Co is grown below 100 °C, followed by the deposition of the main Co layer at 500 °C–600 °C. This approach eliminates the low sticking issue at high temperatures, because Co sticks to preexisting particles of the seeding layer. The coalescence of islands grown at 600 °C is shown to be of the liquidlike type, which explains why the spatial ordering along the steps is lost at higher exposures.

Crystal structure, epitaxial relations, and defects of Co nanoparticles have been studied by different diffraction methods. Analysis of RHEED data shows that the best crystalline quality is obtained above 500 °C. The fcc crystal structure continuing the lattice of CaF_2 is found to be dominant. Unusual streaks with rather slow intensity decay rates are observed by RHEED. The XRD analysis shows that the main reason for streaking is the antiphase domain boundaries. The HRTEM studies confirm the presence of those boundaries and also show that the Co/CaF_2 interface is abrupt with no intermixing. The geometrical shape of the Co islands, examined by AFM, SEM, and TEM, is shown to be flat topped and faceted with {111} and {100} crystal planes.

It has been found that magnetic and magneto-optical properties depend strongly on the density and shape of Co nanoparticles. The transition from dense to dilute arrays leads to the change of in-plane and out-of-plane magnetic anisotropy as well as the signs of PMOKE and LMOKE. In the structures with linear chains of Co nanoparticles, the in-plane magnetic anisotropy behaves similarly to quasi-one-dimensional Fe/W(110) (Ref. 56) and Fe/Mo(110) (Ref. 57) stripes, but differently to the Fe/Cu(111) stripes, where the easy axis is perpendicular to the surface.[58] It is also shown that the magnetodipole interaction plays an important role in

the magnetic properties of structures with Co exposure higher than 10 nm. This leads to a strong in-plane magnetic anisotropy in the spatially ordered arrays.

A wide range of characterization techniques (including the direct space and reciprocal space methods) used in this study along with growth modeling have led to a good understanding of a rather complex growth process in this important material system. The kinetic tuning knobs have been identified that enable precise control over the growth of Co nanoparticles at different stages, including the CaF_2 layer deposition, Co nucleation, growth, and coalescence. Important correlations between the morphology, crystal structure, and magnetic properties have been revealed. More studies are planned to identify the role of elastic relaxation and plastic deformation in the resulting structures.[59] A wide range of implementations of the achieved understanding is expected, including the controlled fabrication of magnetic nanoparticles not only on the nonmagnetic insulators such as CaF_2, but also on magnetically ordered materials like antiferromagnetic MnF_2 and NiF_2.

ACKNOWLEDGMENTS

This work was partially supported by the grants of the Russian Ministry of Education and Science (Grant Agreement No. 8368) and the Russian Foundation for Basic Research, as well as the scientific programs of the Russian Academy of Sciences. N.S.S. and S.M.S. wish to acknowledge the University of Nagoya (Japan). XRD experiments were carried out under Projects No. 2007G199 and No. 2010G190 at Photon Factory. The authors appreciate the assistance of A. K. Kaveev in preparation of samples. SEM and TEM characterization of the samples have been carried out in the Joint Research Center "Materials science and characterization in advanced technologies" operating under financial support of the Russian Ministry of Education and Science.

*nsokolov@fl.ioffe.ru

[1] J. A. Venables, G. D. T. Spiller, and M. Hanbucken, Rep. Prog. Phys. **47**, 399 (1984).
[2] J. Robins, Appl. Surf. Sci. **33-34**, 379 (1988).
[3] J. Zhou, Y. C. Kang, and D. A. Chen, Surf. Sci. **537**, L429 (2003).
[4] K. Fujikawa, S. Suzuki, Y. Koike, W.-J. Chun, and K. Asakura, Surf. Sci. **600**, 117 (2006).
[5] K. Højrup-Hansen, S. Ferrero, and C. Henry, Appl. Surf. Sci. **226**, 167 (2004).
[6] C. Mocuta, A. Barbier, G. Renaud, and B. Dieny, Thin Solid Films **336**, 160 (1998).
[7] F. Silly and M. R. Castell, Appl. Phys. Lett. **87**, 053106 (2005).
[8] D. Chen, M. Bartelt, R. Hwang, and K. McCarty, Surf. Sci. **450**, 78 (2000).
[9] K. R. Heim, S. T. Coyle, G. G. Hembree, J. A. Venables, and M. R. Scheinfein, J. Appl. Phys. **80**, 1161 (1996).
[10] N. Mattoso, D. H. Mosca, W. H. Schreiner, I. Mazzaro, and S. R. Teixeira, Thin Solid Films **272**, 83 (1996).
[11] N. L. Yakovlev, A. K. Kaveev, N. S. Sokolov, B. B. Krichevtsov, and A. Huan, Curr. Appl. Phys. **6**, 575 (2006).
[12] L. Pasquali, B. P. Doyle, F. Borgatti, A. Giglia, N. Mahne, M. Pedio, S. Nannarone, A. K. Kaveev, A. S. Balanev, B. B. Krichevtsov, S. M. Suturin, and N. S. Sokolov, Surf. Sci. **600**, 4170 (2006).
[13] Y. Shiratsuchi, M. Yamamoto, and S. D. Bader, Prog. Surf. Sci. **82**, 121 (2007).
[14] M. R. Scheinfein, K. E. Schmidt, K. R. Heim, and G. G. Hembree, Phys. Rev. Lett. **76**, 1541 (1996).
[15] A. Paul, T. Damm, D. E. Burgler, S. Stein, H. Kohlstedt, and P. Grunberg, J. Phys.: Condens. Matter **15**, 2471 (2003).
[16] J. Nogués, J. Sort, V. Langlais, V. Skumryev, S. Suriñach, J. S. Muñoz, and M. D. Baró, Phys. Rep. **422**, 65 (2005).
[17] S. M. Suturin, V. V. Fedorov, A. G. Banshchikov, D. A. Baranov, K. V. Koshmak, P. Torelli, J. Fujii, G. Panaccione, K. Amemiya, M. Sakamaki, T. Nakamura, M. Tabuchi, L. Pasquali, and N. S. Sokolov, J. Phys.: Condens. Matter **25**, 046002 (2013).
[18] V. G. Dubrovskii, G. E. Cirlin, Y. G. Musikhin, Y. B. Samsonenko, A. A. Tonkikh, N. K. Polyakov, V. A. Egorov, A. F. Tsatsul'nikov, N. A. Krizhanovskaya, V. M. Ustinov, and P. Werner, J. Cryst. Growth **267**, 47 (2004).
[19] V. V. Afrosimov, R. N. Il'in, V. I. Sakharov, I. T. Serenkov, D. V. Yanovskii, S. F. Karmanenko, and A. A. Semenov, Phys. Sol. State **41**, 527 (1999).
[20] N. S. Sokolov and S. M. Suturin, Thin Solid Films **367**, 112 (2000).
[21] N. S. Sokolov, J. C. Alvarez, Y. V. Shusterman, N. L. Yakovlev, R. M. Overney, Y. Itoh, I. Takahashi, and J. Harada, Appl. Surf. Sci. **104**, 402 (1996).
[22] V. G. Dubrovskii and M. V. Nazarenko, J. Chem. Phys. **132**, 114507 (2010).
[23] V. G. Dubrovskii, Phys. Stat. Solidi B **238**, R1 (2003).
[24] V. G. Dubrovskii, G. E. Cirlin, and V. M. Ustinov, Phys. Rev. B **68**, 075409 (2003).
[25] A. D. Gates and J. L. Robins, Surf. Sci. **116**, 188 (1982).
[26] K. Yamamoto, T. Iijima, T. Kunishi, K. Fuwa, and T. Osaka, J. Cryst. Growth **94**, 629 (1989).
[27] J. A. Venables, L. Giordano, and J. H. Harding, J. Phys.: Condens. Matter **18**, S411 (2006).
[28] M. J. J. Jak, C. Konstapel, A. van Kreuningen, J. Chrost, J. Verhoeven, and J. W. M. Frenken, Surf. Sci. **474**, 28 (2001).
[29] B. W. Lee, R. Alsenz, A. Ignatiev, and M. A. Van Hove, Phys. Rev. B **17**, 1510 (1978).
[30] A. N. Kolmogorov, Cl. Sci. Math. Nat. **3**, 355 (1937).
[31] V. G. Dubrovskii, N. V. Sibirev, J. C. Harmand, and F. Glas, Phys. Rev. B **78**, 235301 (2008).
[32] A. I. Persson, M. W. Larsson, S. Stenström, B. J. Ohlsson, L. Samuelson, and L. R. Wallenberg, Nat. Mater. **3**, 677 (2004).
[33] K. W. Ng, W. S. Ko, T.-T. D. Tran, R. Chen, M. V. Nazarenko, F. Lu, V. G. Dubrovskii, M. Kamp, A. Forchel, and C. J. Chang-Hasnain, ACS Nano **7**, 100 (2013).
[34] S. Ferrer, J. Alvarez, E. Lundgren, X. Torrelles, P. Fajardo, and F. Boscherini, Phys. Rev. B **56**, 9848 (1997).
[35] E. Gu, S. Hope, M. Tselepi, and J. A. C. Bland, Phys. Rev. B **60**, 4092 (1999).
[36] G. Baudot, Y. Girard, V. Repain, S. Rohart, S. Rousset, S. Kreckelbergh, A. Coati, and Y. Garreau, Surf. Sci. **557**, 171 (2004).

[37]S. M. Valvidares, T. Schroeder, O. Robach, C. Quirós, T.-L. Lee, and S. Ferrer, Phys. Rev. B **70**, 224413 (2004).
[38]C.-S. Yoo, P. Söderlind, and H. Cynn, J. Phys.: Condens. Matter **10**, L311 (1998).
[39]D. P. Dinega and M. G. Bawendi, Angew. Chem., Int. Ed. **38**, 1788 (1999).
[40]Y. K. Su, C. M. Shen, T. Z. Yang, H. T. Yang, H. J. Gao, and H. L. Li, Appl. Phys. A **81**, 569 (2004).
[41]S. Sun and C. B. Murray, J. Appl. Phys. **85**, 4325 (1999).
[42]L. Pasquali, S. M. Suturin, V. P. Ulin, N. S. Sokolov, G. Selvaggi, A. Giglia, N. Mahne, M. Pedio, and S. Nannarone, Phys. Rev. B **72**, 045448 (2005).
[43]E. Lundgren, J. Alvarez, X. Torrelles, K. F. Peters, H. Isern, and S. Ferrer, Phys. Rev. B **59**, 2431 (1999).
[44]Z. Kovats, M. Rauscher, H. Metzger, J. Peisl, R. Paniago, H.-D. Pfannes, J. Schulze, I. Eisele, F. Boscherini, and S. Ferrer, Phys. Rev. B **62**, 8223 (2000).
[45]C. A. F. Vaz, J. A. C. Bland, and G. Lauhoff, Rep. Prog. Phys. **71**, 056501 (2008).
[46]B. Kalska, J. J. Paggel, P. Fumagalli, M. Hilgendorff, and M. Giersig, J. Appl. Phys. **92**, 7481 (2002).
[47]B. Kalska, K. Schwinge, J. Paggel, P. Fumagalli, M. Hilgendorff, and M. Giersig, J. Appl. Phys. **98**, 044318 (2005).
[48]S. Thamm and J. Hesse, J. Magn. Magn. Mater. **154**, 254 (1996).
[49]S. Thamm and J. Hesse, J. Magn. Magn. Mater. **184**, 245 (1998).
[50]O. Henkel, Phys. Stat. Solidi **7**, 919 (1964).
[51]J. García-Otero, M. Porto, and J. Rivas, J. Appl. Phys. **87**, 7376 (2000).
[52]B. B. Krichevtsov, S. V. Gastev, D. S. Il'yushchenkov, A. K. Kaveev, and N. S. Sokolov, Phys. Solid State **51**, 118 (2009).
[53]B. B. Krichevtsov, A. K. Kaveev, A. Balanev, N. S. Sokolov, J. Camarero, and R. Miranda, Phys. Solid State **49**, 1481 (2007).
[54]L. D. Buda, I. L. Prejbeanu, M. Demand, U. Ebels, and K. Ounadjela, IEEE Trans. Magn. **37**, 2061 (2001).
[55]R. K. Dumas, D. A. Gilbert, N. Eibagi, and K. Liu, Phys. Rev. B **83**, 060415 (2011).
[56]J. Hauschild, H. J. Elmers, and U. Gradmann, Phys. Rev. B **57**, R677 (1998).
[57]P. Jubert, O. Fruchart, and C. Meyer, J. Magn. Magn. Mater. **245**, 565 (2002).
[58]J. Shen, J. P. Pierce, E. W. Plummer, and J. Kirschner, J. Phys.: Condens. Matter **15**, R1 (2003).
[59]X. Zhang, V. G. Dubrovskii, N. V. Sibirev, and X. Ren, Cryst. Growth Des. **11**, 5441 (2011).